A terahertz band-pass resonator based on enhanced reflectivity using spoof surface plasmons

Jingbo Liu, Rajind Mendis and Daniel M Mittleman[1]

Department of Electrical and Computer Engineering, MS 378, Rice University, Houston, TX 77251–1892, USA
E-mail: daniel@rice.edu

Abstract. We demonstrate a band-pass resonator in the terahertz (THz) range, based on a frequency-selective designer reflector. The resonator consists of a parallel-plate waveguide, a designed groove pattern cut into the output facet of each plate, and a reflecting mirror. The patterned facet supports a spoof surface plasmon mode, which modifies the reflectivity at the waveguide output facet by interacting with the waveguide mode. By tuning the geometrical parameters of the groove pattern, the reflectivity at the patterned output facet can be increased up to ∼100% for a selected frequency. Broadband THz waves are quasi-optically coupled into this resonator and reflected multiple times from the patterned facet. This leads to a narrowing of the spectrum at the selected frequency. The *Q* value of the resonator increases as the number of reflections on the patterned facet increases, reaching ∼25 when the THz wave has experienced 12 reflections.

[1] Author to whom any correspondence should be addressed.

IOP Institute of Physics ⏀ DEUTSCHE PHYSIKALISCHE GESELLSCHAFT

Contents

1. Introduction

Theoretically, bound surface waves are not supported on the surface of a perfect metal with infinite conductivity. Therefore, practically, in spectral regimes where metals become highly conducting, surface waves are only weakly bound. However, by adding structure to an otherwise smooth metal surface, it becomes possible for the surface to support a tightly bound surface wave, known as a spoof surface plasmon (SSP) [1–4]. The characteristics of propagation and confinement of the electromagnetic waves on a corrugated perfect metal surface are closely analogous to those of the surface plasmon waves on a metal with finite conductivity, which is excited by the interaction of electromagnetic waves with free electrons on the surface. A promising aspect of SSPs is that their properties can be controlled in a range of frequencies by changing the geometry of the patterned structures [5, 6]. This concept is especially important in the terahertz (THz) range where the metallic conductivity is very high for most common metals leading to weakly bound surface waves (e.g. [7–12]). Thus the concept of SSPs has attracted a great deal of recent interest in applications such as squeezing a THz beam into a subwavelength volume [4, 13], enhancing transmission through a subwavelength aperture or slit [14–17] or improving the collimation of the spatial mode of a THz quantum cascade laser [18, 19].

     Many of these previous studies involving THz SSPs have been focused on enhancing transmission through a subwavelength structure; the idea of using SSPs for enhancing reflection has not been explored. Recently, we described an approach for engineering a high reflectivity (>99%) at the output facet of a parallel-plate waveguide (PPWG) by using subwavelength structures on the waveguide's output facet [20]. We choose a PPWG as a design platform because of its popularity as a prototype guided wave structure in the THz region. With a TEM mode having no cut-off, negligible group velocity dispersion, and low ohmic losses, the PPWG has proven to be a useful platform for many applications involving THz pulses [21–25]. As is well known, an abruptly terminated PPWG exhibits a reflection at the output end, resulting from an impedance mismatch between the waveguide and free space [26, 27]. Although there is no simple analytic description for the strength of this reflection as a function of the spacing between the parallel plates, we have recently characterized it using experimental measurements [27], and exploited its sensitivity to near-field effects for subwavelength imaging [26]. For a large plate spacing ($b > \lambda$), the effective impedance of the PPWG is close to the impedance of free space Z_0 (~377 Ω), and as a result there is almost no reflection. For a small plate spacing ($b < \lambda$), the effective impedance of the PPWG decreases proportionally to the plate spacing b, and thus
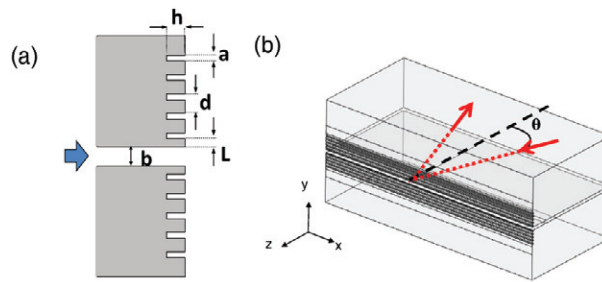
Figure 1. (a) Illustration of the groove pattern on both plates, shown in cross-section. The geometrical parameters h, a, d, L and b are defined in the figure. (b) A 3D rendering of the PPWG with grooves cut on the output facet. The red trace shows one possible trajectory of the incident beam and reflected beam with respect to the normal to the output facet.

the reflection resulting from the impedance mismatch increases as b decreases, approaching unity if b is much smaller than the wavelength λ [26, 27]. When an appropriate structure is cut into the output facet of the PPWG, another mode propagating on the output facet (the SSP mode) is introduced into the interplay and could lead to a significant change of the reflection coefficient [20]. In this study we discuss how to choose geometrical parameters in order to create a high reflector ($R > 99\%$) and we characterize the effect of oblique incidence at the output facet for this enhanced reflectivity.

Narrow-band resonators or filters have always been an interesting research area in the THz range, because of their applications in many areas of THz technologies, such as in wireless communications [28] and sensing [29, 30]. A few methods have been used to implement THz resonators, including quasi-optic resonators based on a Fabry–Perot cavity [30, 31], membrane resonators using metamaterials [32], wire-disc resonators which rely on whispering gallery modes [33], integrated waveguide-coupled THz resonators using microcavities [34–36], Bragg gratings with defects [29, 37, 38] and various types of quantum-cascade lasers [39–41]. Here, we demonstrate a prototype of a band-pass THz resonator by using the concept of a designer reflector.

2. Enhanced reflection using spoof surface plasmons

2.1. Design and modeling

Our device is based on an aluminum PPWG. To support SSPs on the output surface, a periodic pattern of straight grooves are cut into the output facet of both the upper and lower waveguide plates, parallel to the output aperture of the waveguide. The groove patterns on the two waveguide plates are identical to each other. Figure 1(a) illustrates a cross-section of a pattern of five periodic grooves on the output facet, adjacent to the waveguide's exit aperture. The cross-section of a single groove is rectangular, with a fixed width (a) of 152 μm. The plate spacing (b), groove depth (h), periodicity (d) and the distance from the first groove to the waveguide aperture edge (L) are varied to tune the frequency and strength of the surface plasmon coupling [1, 3, 11, 18, 19]. Figure 1(b) shows a perspective rendering of an assembled waveguide structure with semi-transparent surfaces. Grooves are visible on the upper and lower plates on the output facet.
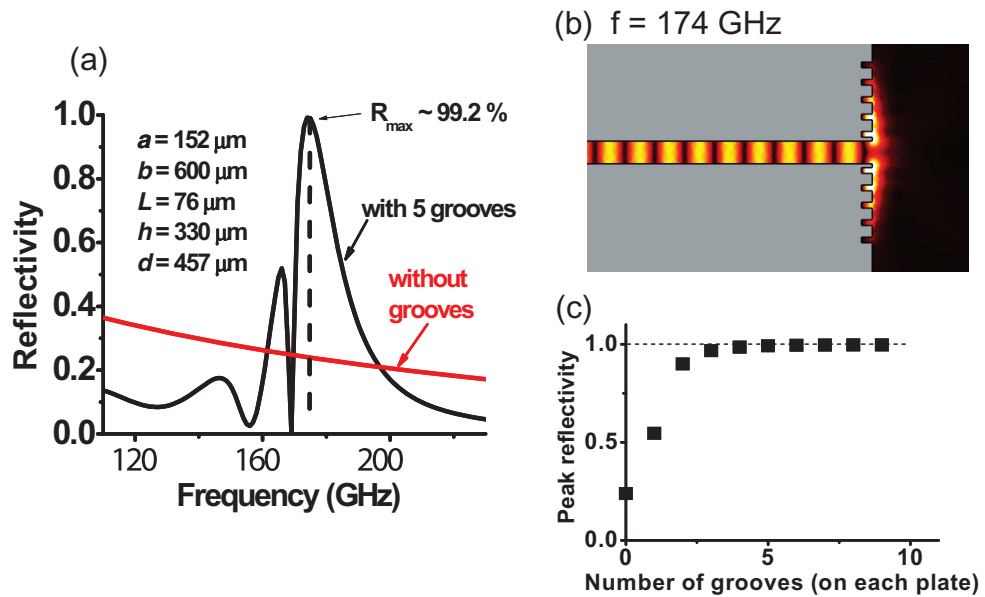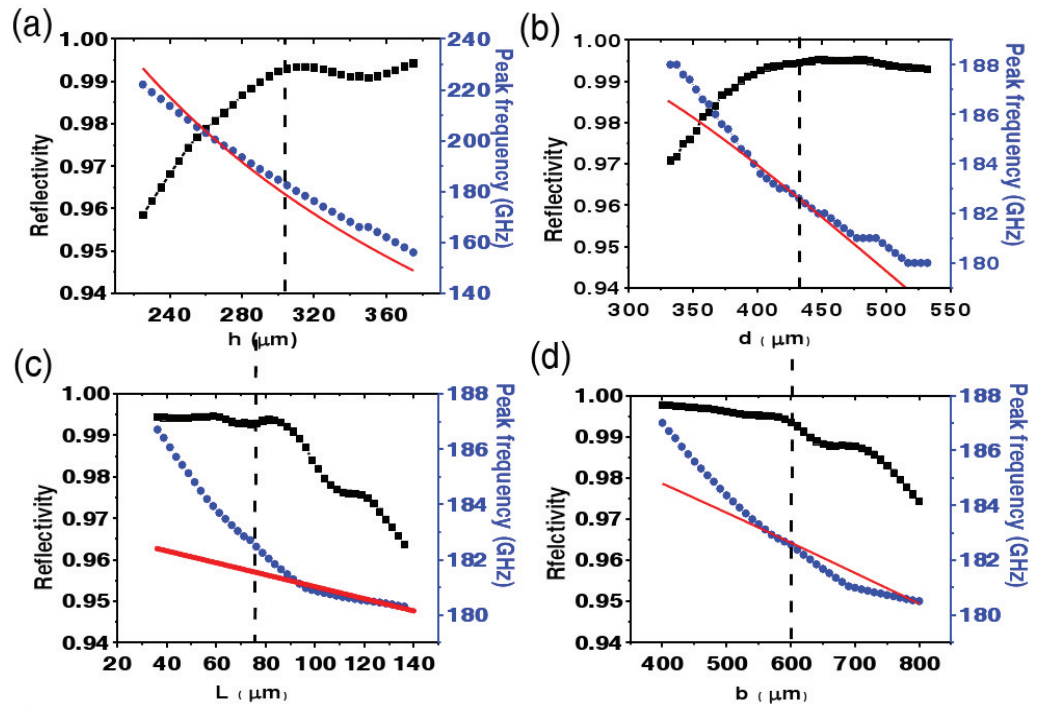
Figure 2. (a) Simulated reflectivity as a function of frequency for the PPWG with the groove pattern defined by the parameters indicated in the inset. The red curve shows the reflectivity of the same waveguide except with no grooves. (b) A false-color plot of the electric field amplitude adjacent to the output aperture of the PPWG at the selected resonant frequency. (c) Peak reflectivity as a function of the number of grooves on each plate.

The red arrow shows a possible ray path of a THz wave reflected from the waveguide output surface at an angle θ.

To fine tune the geometrical parameters of the groove pattern for the highest reflectivity, we conducted numerical simulations using the finite element method (FEM) [42]. Figure 2(a) shows an example of the optimized reflectivity. The plot illustrates the simulated reflection coefficients as a function of frequency with the parameter settings as indicated in the inset. At the selected frequency (174 GHz), the reflection coefficient at the output facet reaches a peak of more than 99% (peak reflectivity). The red curve shows a simulation using the same PPWG without groove patterns on the output surface, in comparison to the case with five grooves on each plate. Clearly, the reflection is greatly enhanced relative to that of a waveguide without any groove pattern (which is ~20% for this plate separation). Figure 2(b) shows a cross-sectional plot of the electric field distribution in the neighborhood of the output aperture at the design frequency (174 GHz). Most of the energy concentrates in the near field in the vicinity of the grooves and the output face of the waveguide, showing no energy coupling out into the far field. The number of grooves on each plate of the PPWG also has an influence on the reflectivity, as shown in figure 2(c). As the number of grooves increases, the peak reflectivity increases to nearly 100%, saturating when the number is larger than about four. Evidently, almost all of the contribution to the enhanced reflectivity is from the first five grooves, so for our experimental studies discussed below we choose to cut five grooves on each plate of the PPWG.

Further simulations permit us to investigate the dependence of this enhanced reflectivity (R) on various aspects of the groove pattern geometry. These simulations are an important aspect

Figure 3. The reflectivity (black squares) and peak frequency (blue circles) as a function of (a) groove depth, (b) groove periodicity, (c) the distance between the first groove and the edge of output aperture and (d) the plate spacing. In these simulations, one parameter is varied while all of the other parameters are fixed at the values shown in figure 2(a).

of the fabrication and optimization process. Figure 3 illustrates the enhanced reflectivity as a function of several relevant geometrical parameters (h, d, L and b as defined in figure 1), extracted from numerical simulations. In figure 3, each panel illustrates the results of a series of simulations in which we sweep the value of a single parameter in a range around the optimized value (indicated by the dashed line in each panel), with the other geometrical parameters fixed at the values indicated in figure 2(a). Two key factors are extracted from the simulations and plotted in this figure: one is the highest value of the reflectivity R exhibited at any frequency within the simulation range, and the other is the frequency at which R reaches this maximum value (labeled as the peak frequency).

As shown in figure 3(a), both the peak frequency and reflectivity are very sensitive to the groove depth (h). This can be understood by using the asymptotic frequency ($\omega = \pi c/2h$) of the SSPs [2], which is designed to enhance reflectivity at the open end of the waveguide. When the groove depth becomes shallower, the asymptotic frequency blue shifts, and thus the SSPs with the same surface confinement have a higher frequency. The periodicity (d) of the pattern also influences the behavior of the supported SSPs, but with less sensitivity than h (as in figure 3(b)). The SSPs have an effective wave vector k_x parallel to the metal surface. For the one-dimensional groove pattern, k_x can be approximately expressed by the dispersion relation [2, 3]

$$k_x = k_0\sqrt{1 + \frac{a^2}{d^2}\tan^2 k_0 h}, \tag{1}$$
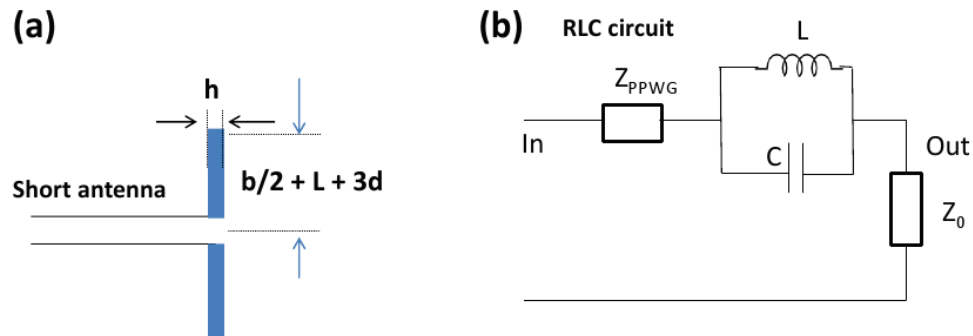
Figure 4. (a) A schematic of the antenna model discussed in the text. (b) The equivalent RLC circuit for the antenna model.

where k_0 is the wave vector in vacuum, and a, h and d are the groove width, groove depth and the periodicity of the groove pattern, respectively. The periodic grooves also act like a grating with a band edge determined by $k_{x1} = \pi/d$. This grating resonance also contributes to the resonant coupling between the waveguide mode and the SSP mode. The periodicity d decreases as the inverse of the band edge k_{x1}, corresponding to a high frequency on the dispersion curve (figure 3(b)). The distance between the first groove and the edge of the waveguide aperture (L) also influences the interaction between the SSP mode and waveguide mode. The longer the distance L, the less the coupling between waves of the two modes, and therefore the less reflectivity. We note that this behavior is not linear, but rather exhibits a threshold behavior, with a rapid decrease in reflectivity for L larger than about 90 μm (figure 3(c)). The plate spacing (b) influences the effective impedance of the TEM mode in the PPWG [26, 27], as well as the diffraction of the waves at the output aperture. Because the enhanced reflection results from the resonant coupling of two modes which have wave vectors orthogonal to each other [20], the coupling efficiency depends on the mode matching at the output of the waveguide. The smaller the plate spacing, the more the waves at the output aperture are strongly diffracted, and thus the better coupling to the modes with orthogonal wave vectors, leading to a larger enhanced reflectivity (figure 3(d)). It is clear from these simulations that, within the tolerance of mechanical machining ($\sim \pm 25$ μm), it is possible to design and fabricate waveguides with groove patterns optimized for high reflectivity ($>99\%$) at a selected frequency of interest. Small errors in the groove geometrical parameters can be offset by slightly adjusting the plate spacing b so as to obtain the desired resonant frequency for maximum reflectivity.

We can gain a qualitative understanding of the dependence of the peak frequency on the geometrical parameters of the groove structure using a simple RLC circuit model (figure 4). Because the plate spacing b of the PPWG and the sizes of the grooves are subwavelength in scale, the whole structure can be represented as a short dipole antenna as illustrated in figure 4(a). In this picture, the PPWG acts as the feeding circuit and the corrugated output facet acts as the antenna pad. The equivalent circuit model is shown in figure 4(b). To analyze this model, we write the effective length of one arm of the dipole antenna as $x = b/2 + L + \eta d$, which is equivalent to the physical size of the corresponding waveguide structure. Here, η represents the number of grooves in which the SSP field amplitude is significant. As shown in figures 2(b) and (c), when the waveguide mode and the SSP mode are resonant, most of the energy concentrates on the first three grooves, so we estimate $\eta \sim 3$. In this case, the capacitance
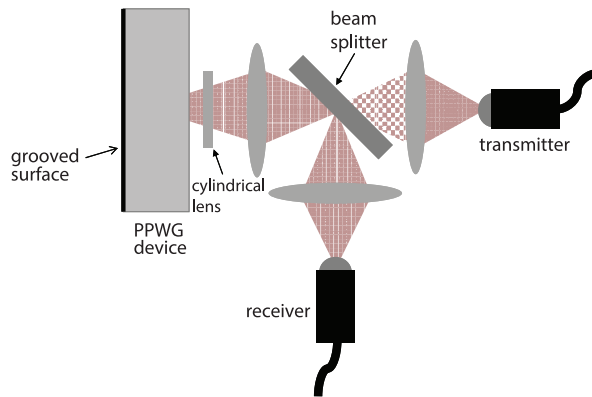
Figure 5. The experimental setup for normal-incidence reflection measurements.

of the structure can be approximated as that of a linear dipole antenna [43, 44]

$$C \approx \frac{\pi \varepsilon_0 x}{\log (x/h)}.$$

(2)

The inductance of the short antenna can be calculated as the ratio of the magnetic flux φ to the current I. According to the numerical simulation, when the waveguide and SSP are at resonance, most of the magnetic field lines are concentrated inside the grooves. The magnetic flux can thus be estimated by using the average magnetic field times the area of the grooves ($\eta a h$). Since the antenna current is fed by the PPWG, it is not influenced by the groove structure and is therefore a constant value. Thus, the inductance is approximately proportional to the groove area. For the circuit of figure 4(b), the resonant frequency is calculated as $\omega = 1/\sqrt{LC}$. From this, we find an approximate proportionality which predicts the scaling of the resonant frequency with geometrical parameters

$$\omega \propto \sqrt{\frac{\log (x/h)}{\eta a h \pi \varepsilon_0 x}}.$$

This expression can be used to understand the functional dependence of the resonant (peak) frequency on the geometrical parameters h, b, L and d. As illustrated by the red curves in figure 3, the predictions of this simple analytical model, with a suitably chosen proportionality constant, show reasonable consistency with the FEM numerical simulations.

2.2. Measurements—normal incidence

The schematic of the experimental setup for the normal-incidence reflectivity measurement is shown in figure 5. A THz-TDS system using a fiber-coupled transmitter and receiver are used, with a bandwidth ranging from 0.05 to 2 THz. The THz wave is polarized normal to the aluminum plates in order to excite the TEM mode at the input of the waveguide. A Teflon cylindrical lens is held adjacent to the input aperture of the PPWG to improve the coupling efficiency into and out of the PPWG [45]. A 2 cm thick high-resistivity silicon beam splitter is used to sample part of the reflected beam into the THz receiver. We use a thick silicon beam splitter so that its etalon reflections can be temporally separated from the signal of interest. The reflected signal from the output facet of the PPWG is measured by the receiver with a long time window to achieve high spectral resolution. Since the incident and reflected beams
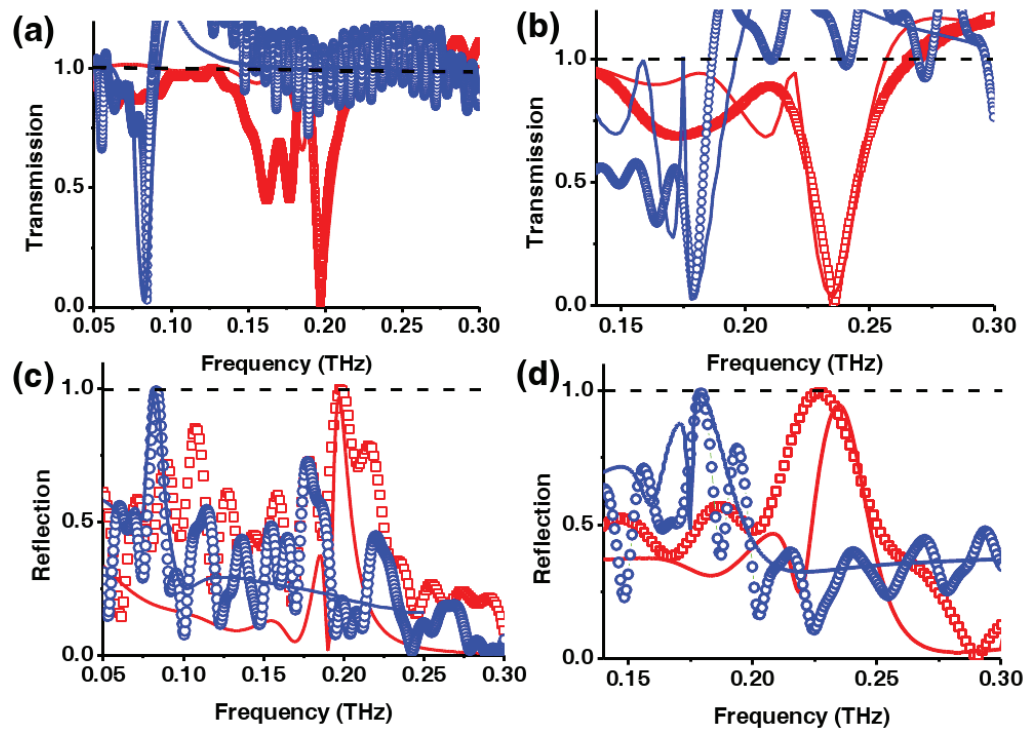
Figure 6. (a) Normalized transmission spectra for the devices of plate spacing $600\,\mu$m with designed resonant frequencies at $83\,$GHz ($h = 736.6\,\mu$m, $L = 50.8\,\mu$m, $d = 301\,\mu$m) and $197\,$GHz ($h = 274.3\,\mu$m, $L = 101.6\,\mu$m, $d = 457.2\,\mu$m). (b) Normalized transmission spectra for devices of plate spacing $200\,\mu$m with designed resonant frequencies at $179\,$GHz ($h = 314.9\,\mu$m, $L = 279.4\,\mu$m, $d = 457.2\,\mu$m) and $234\,$GHz ($h = 205.7\,\mu$m, $L = 228.6\,\mu$m, $d = 457.2\,\mu$m). (c) Normalized reflection spectra for the same devices as (a). (d) Normalized reflection spectra for the same devices as (b). In all four panels, the squares and circles indicate the experimental results, while the solid lines show the results of the corresponding numerical simulations.

are overlapped and are normal to the PPWG output face, the measured signal is the normal reflection as indicated in figure 5.

A series of waveguides with each plate having a five-rectangular-groove pattern of different parameters were fabricated and tested in our setup. Figure 6 shows typical examples of transmission and reflection for two sets of waveguides. One set has a plate spacing of $b = 600\,\mu$m (figures 6(a) and (c)), while the other has a separation of $200\,\mu$m (figures 6(b) and (d)). The transmitted signals are collected by putting the receiver on the optical axis $2\,$cm away from the output of the waveguide. These transmission spectra are normalized to the transmission spectra through a waveguide of identical dimensions without grooves. For reflection, a reference signal was measured by pressing an aluminum mirror directly against the output facet, so that the reference signal represents a nearly perfect reflection at the output facet.

For the waveguide of plate spacing of $600\,\mu$m, two different five-groove patterns are tuned (by choosing L, h and d) for two distinctive frequencies, 83 and $197\,$GHz. Figures 6(a) and (c) show that the transmission is strongly diminished and the reflection enhanced ($> 99\%$) at the
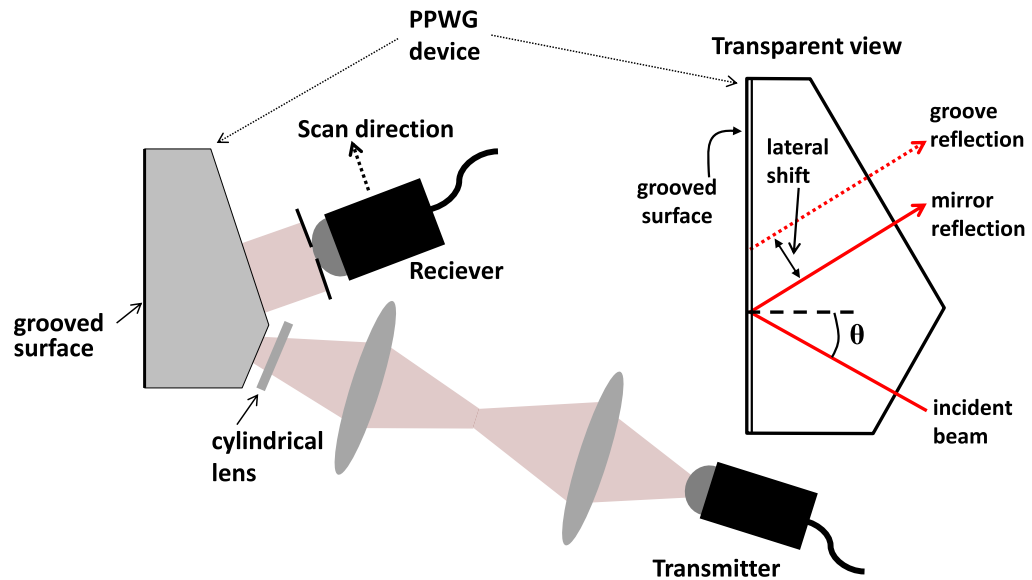
Figure 7. Experimental setup for the measurement of reflection at an oblique angle of incidence, $\theta > 0$. The right inset shows a ray tracing schematic of the device designed for the measurement of the lateral spatial shift of the reflected beam as a function of angle of incidence.

design frequencies for both cases. These results are in reasonable agreement with numerical simulations (solid curves), except for small oscillations in the measured spectra resulting from multiple reflections in the THz optics. For waveguides of plate spacing of $200\,\mu$m, the groove patterns are also optimized for two different frequencies, 179 and 234 GHz. Similar strong modifications of the spectrum are shown in figures 6(b) and (d), which also shows a reflection coefficient approaching 100%. These results demonstrate that the peak frequency can be tuned by modifying the geometrical parameters of the metal surface structuring, while maintaining the near-perfect reflection at the design frequency.

We note that a PPWG which has a plate spacing of $200\,\mu$m exhibits a reflection at the output aperture of $\sim$60% even with no groove pattern, because of the impedance-matching consideration discussed above [26, 27]. Thus to differentiate the reflectivity enhancement by SSPs, it is clearer to use PPWGs of spacing $600\,\mu$m, for which the reflection coefficient is less than 20% at the frequencies of interest when the output facet is not patterned with grooves. In this case of larger plate spacing, the reflectivity change (grooves vs. no grooves) is more than a factor of five.

2.3. Angle dependence and phase shifts

An interesting approach to understand the enhanced reflectivity induced by SSPs is to probe the resonant coupling between the TEM mode in the PPWG and the surface plasmon mode on the patterned surface by varying the incident angle (θ) (see figure 1). For these angle-dependent measurements, we need to fabricate a new series of waveguides with an angled facet on the input side, so that the input and reflected waves both travel through a waveguide facet that is normal to the propagation direction (as shown in the inset of figure 7). We fabricate a series of waveguides, all of which have identical groove patterns, but each of which has a different angle cut on the
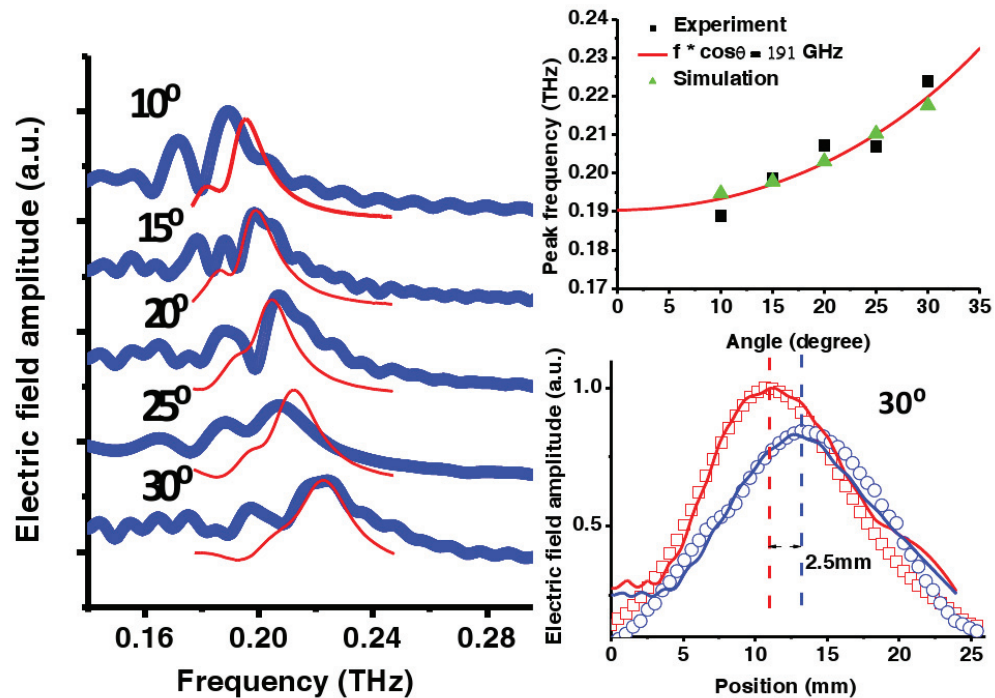
Figure 8. The spectra of the reflected signals at different incident angles. Blue lines represent the experimental results and the red lines represent FEM simulations. The top right inset shows the peak frequency as a function of incident angle, from experiment, simulation, and a simple model, all showing good agreement. The bottom right inset shows the lateral shift of the reflected signals for a typical angle of incidence (30°), from both experiments and numerical simulations.

input facet. In this way, we can study the angle dependence of the reflection without having to disentangle effects at the non-patterned input facet. For these measurements, the groove pattern was designed to have a maximum reflectivity at a frequency of 191 GHz when excited at normal incidence ($\theta = 0$). For each incident angle, the THz receiver was masked by a 1 mm aperture and placed 2 cm away from the waveguide facet where the reflected wave emerges.

As indicated in figure 8, the peak frequency at which the reflection reaches a maximum shifts as the incident angle increases. This is consistent with the three-dimensional (3D) FEM simulation, shown as red curves in figure 8. The peak frequency shifts according to $f_{peak} = f_0/\cos\theta$, where f_0 is the design frequency for normal incidence (191 GHz) that is determined by the groove geometry. A plot of this dependence is shown in the top right panel in figure 8 along with the experimental and simulation results, all of which show good agreement. The origin of the angle dependence can be explained by a model based on the coupling between the surface mode and the component of the waveguide mode perpendicular to the output facet, as discussed previously [20].

In addition to an angle-dependent frequency shift, another phenomenon associated with the SSP reflection is an angle-dependent spatial shift of the output beam. This lateral shift is shown in the bottom right panel in figure 8. It is measured by scanning the receiver (figure 7) along a line parallel to the waveguide facet from which the beam emerges and 2 cm away

from this facet. In figure 8, the data points show the amplitude of the reflected wave at the frequency of maximum reflection as a function of position along this line. The red squares show the result when a mirror is pressed against the output facet while the blue circles show the reflection from the patterned output facet. The solid curves show the corresponding numerical simulation results. A lateral shift of 2.5 mm is observed for the incident angle of 30°. This shift is strongly reminiscent of the Goos–Hänchen effect discussed initially in the context of total internal reflection [46–48]. A lateral shift is a general consequence of a reflection from an interface where the beam has a finite width and the amplitude reflection coefficient is complex. A distinction between the lateral shift observed here and the traditional Goos–Hänchen effect is that in our case, the shift arises from an interaction with a surface wave whose wave vector is perpendicular to the plane of incidence [20].

Finally, we also observe a decrease in the maximum value of the reflectivity with increasing angle. As the angle of incidence increases, the maximum reflectivity decreases from almost 99% at 10° to 84% at 30°. This change in the reflectivity is an important property and should be considered in its further applications, such as the resonator design discussed below. The decrease of maximum reflectivity can be understood qualitatively as follows: when the incident wave has a wave vector component parallel to the groove axis (the *x*-axis shown in figure 1), a portion of the energy can couple to the groove channels, which itself is a waveguide [49, 50], and cause energy loss by propagating along the groove axis. The amount of the energy loss in this way depends on the coupling efficiency which is an increasing function of the incident angle. Therefore the incident angle should be kept low in the application design in order to obtain high reflectivity.

3. A terahertz resonator

The patterned PPWG has a distinctive quality of achieving high reflection ($>99\%$) at a single design frequency, making it a potential candidate for various THz applications. Here, we introduce an example of a THz resonator.

When a broadband THz wave is reflected at the output facet of a PPWG with an engineered groove pattern, it carries almost 100% of the energy at the design frequency (figure 6). Thus the patterned output surface acts as a nearly ideal THz filter, with a full width at half maximum (FWHM) of a few tens of GHz. Cascading of this filter operation will therefore lead to narrowing of the spectrum reflected back into the waveguide, with relatively little loss at the design frequency. Therefore, multiple reflections can be used to design a resonator with a high quality-factor Q and relatively high throughput.

To explore this concept, we first conduct FEM simulations of a structure in which the THz wave reflects three times off of a patterned facet. Figure 9 illustrates top-down views of the results of these simulations. These results display the electric field distributions when the THz beam is incident at an angle of 10° to the normal of the reflecting surfaces. The blue lines indicate the surfaces that are patterned with grooves to provide enhanced reflection. Figure 9(a) shows the result at the design frequency (174 GHz), while figure 9(b) shows the same result except that the grooved surfaces have been replaced in the simulations by perfectly reflecting mirrors at the same locations. For these two cases, we observe that nearly the same energy is delivered to the output port of the device. Figures 9(c) and (d) show the results when the device is excited off resonance. The energy delivered to the output port drops to nearly zero for 160 GHz (figure 9(c)) and 190 GHz (figure 9(d)).
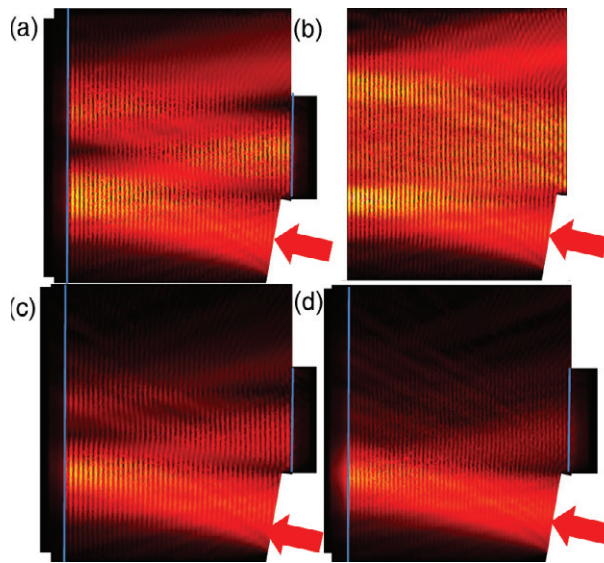
Figure 9. Plots of the electric field distribution (from 3D FEM simulations) inside the devices designed as resonators, with three internal reflections. (a) Device with the same pattern of grooves on both reflecting facets (marked by blue lines) when the input wave is at design frequency (174 GHz). (b) Device with perfect mirrors instead of the groove patterns, at the design frequency. (c) The same device as (a) except the input wave is at frequency 160 GHz. (d) The same device as (a) except the input wave is at frequency 190 GHz.

When using a resonator based on the geometry shown in figure 9, the requirement of two identical groove patterns on both of the reflecting facets poses somewhat of a fabrication challenge. Typical machining tolerances of $\sim$25 μm will lead to uncertainty in the groove geometrical parameters (L, h and d), which will lead to shifts in the peak frequency for one reflecting surface relative to the other one. Obviously, in order for the resonator to operate as anticipated, such shifts are not desirable. Even a small difference in design frequency of less than 10 GHz will lead to a dramatic reshaping of the spectrum of the radiation reaching the output port, especially in the case of a large number of internal reflections. To avoid this problem, we modify the design for the THz resonator as shown in figure 10. Here, only one facet of the waveguide is decorated with grooves, while the other facet relies on a broadband mirror reflection. This firmly contacted mirror makes a perfect reflection at its interface for the THz waves coming from inside the waveguide, creating an image of the groove-patterned facet symmetric to the mirror (as labeled in figure 10). The grooved surface has a length of 15 cm, in order to allow space for multiple reflections between the input and output port. The mirror on the upper facet can be lengthened or shortened, in order to control the number of internal reflections—a longer mirror will give rise to more reflections before the wave reaches a point where it can escape from the device. Therefore the overall result is equivalent to reflection from two identical patterned facets as in figure 9, but without the fabrication challenge of creating two identical groove patterns on two different surfaces.

To demonstrate this resonator, we fabricated the device as shown in figure 10. The groove pattern was designed for a peak frequency of 170 GHz when illuminated at normal incidence, or 167 GHz when illuminated at 10° (as is relevant here). The receiver is placed 2 cm away from
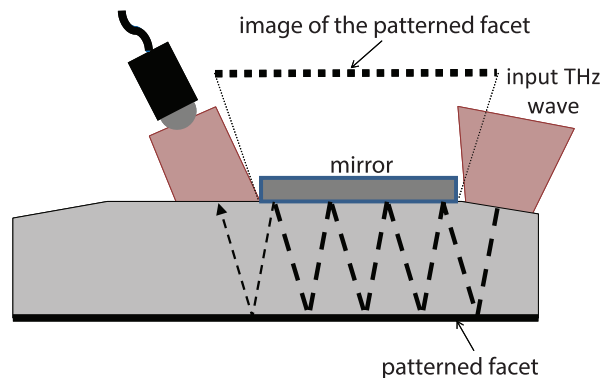
Figure 10. A schematic of the device with a single patterned facet, fabricated for the experimental measurements. The dotted line shows the image of the patterned facet. The dashed line shows a ray path of a multiply reflected THz beam inside the device.
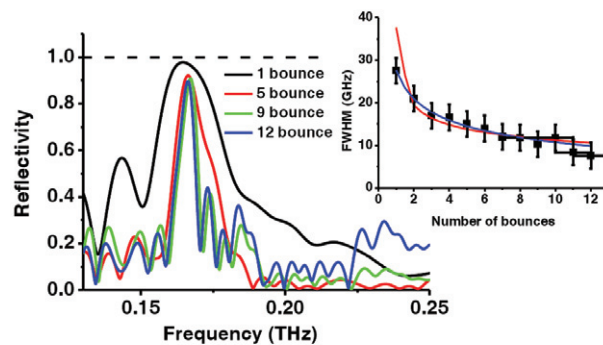
Figure 11. Normalized reflection spectra for the signals after multiple bounces inside the resonator device depicted in figure 10. The inset shows the FWHM of the spectra as a function of the number of internal bounces off of the groove-patterned surface. The red curve shows the FEM simulation, while the blue curve shows a simple calculation extrapolating the line narrowing from the result from a single bounce. The black squares show the experimental results with estimated error bars.

the facet without a groove pattern, adjacent to the contact mirror, to collect the waves emerging from the waveguide. By varying the length of the reflecting mirror and adjusting the location of the receiver, the number of reflections on the patterned facet can be modified and identified in the time domain, since each subsequent reflection adds additional travel path length (and therefore time delay) to the signal. For each measurement, we acquire a reference signal by pressing another mirror tightly against the facet with groove patterns, similar to the procedure used for referencing for the data of figure 6(c) and (d).

The results of these measurements are shown in figure 11. A few typical output spectra are shown, for different numbers of internal reflections. Evidently, the width of the spectral peak decreases as the number of bounces increases, while the peak amplitude only changes by a small amount. We find that the FWHM decreases from ~30 GHz for the case of only 1 reflection to ~7 GHz for 12 reflections. We can understand this line narrowing as a simple cascading filter

IOP Institute of Physics **Φ** DEUTSCHE PHYSIKALISCHE GESELLSCHAFT

effect, as discussed above. To confirm this interpretation, we use the spectrum measured after a single reflection as a starting point, and compute the evolution of the FWHM by considering higher-order multiples of this spectrum. This result is shown as the blue curve in the inset of figure 11, along with the measured widths (data points). These results are also consistent with numerical simulations (red curve).

It is important to note the effects of diffraction. The THz wave is coupled into a PPWG at a beam width of 1.5 cm using a pair of confocal lenses. The path length of the THz wave inside the waveguide after 12 bounces is almost 70 cm. Assuming Gaussian beam diffraction, we would expect a beam waist of ∼9 cm at the output port. Thus, for a large number of reflections, the signal collected at the receiver is actually an overlapping mix of several temporal signals that have experienced differing numbers of reflections. These are reasonably well separated in the time domain because each has traveled a different path length. However, since the filtering effect significantly stretches the original single-cycle pulse in the time domain, the trailing part of one particular reflection can overlap with the leading part of the subsequent reflection. This is essentially an experimental artifact of studying a narrowband effect using a broadband-pulse technology, which leads to some uncertainty in the extraction of, e.g., the precise linewidths (as shown by the error bars in figure 11). We would anticipate that this concern would be largely eliminated if a narrowband tunable THz source were used.

4. Conclusion

In conclusion, we have demonstrated that by using SSPs the reflectivity at the output facet of a PPWG can be enhanced almost up to 100% within a desired THz spectral range. We present a prototype of a THz resonator based on this new concept. This device concept could prove valuable in a variety of applications in which narrowband spectral filtering or sensing is desired, such as for example in the THz analog of cavity ring-down spectroscopy.

Acknowledgment

References

[1] Pendry J B, Martín-Moreno L and Garcia-Vidal F J 2004 Mimicking surface plasmons with structured surfaces *Science* **305** 847–8
[2] Garcia-Vidal F J, Martín-Moreno L and Pendry J B 2005 Surfaces with holes in them: new plasmonic metamaterials *J. Opt. A: Pure Appl. Opt.* **7** 97–101
[3] Maier S A 2007 *Plasmonics: Fundamentals and Applications* (New York: Springer Science+Business Media)
[4] Maier S A, Andrews S R, Martín-Moreno L and Garcia-Vidal F J 2006 Terahertz surface plasmon-polariton propagation and focusing on periodically corrugated metal wires *Phys. Rev. Lett.* **97** 176805
[5] Ozbay E 2006 Plasmonics: merging photonics and electronics at nanoscale dimensions *Science* **311** 189–93
[6] Fu Z, Gan Q Q, Ding Y J and Bartoli F J 2008 From waveguiding to spatial localization of THz waves within a plasmonic metallic grating *IEEE J. Sel. Top. Quantum Electron.* **14** 486–90
[7] Wang K and Mittleman D M 2004 Metal wires for terahertz wave guiding *Nature* **432** 376–9
[8] Jeon T-I, Zhang J and Grischkowsky D 2005 THz Sommerfeld wave propagation on a single metal wire *Appl. Phys. Lett.* **86** 161904

[9] Jeon T-I and Grischkowsky D 2006 THz Zenneck surface wave (THz surface plasmon) propagation on a metal sheet *Appl. Phys. Lett.* **88** 061113

[10] Shen L F, Chen X D and Yang T J 2008 Terahertz surface plasmon polaritons on periodically corrugated metal surfaces *Opt. Express* **16** 3326–33

[11] Williams C R, Andrews S R, Maier S A, Fernandez-Dominguez A I, Martin-Moreno L and Garcia-Vidal F J 2008 Highly confined guiding of terahertz surface plasmon polaritons on structured metal surfaces *Nature Photon.* **2** 175–9

[12] Zhu W Q, Agrawal A and Nahata A 2008 Planar plasmonic terahertz guided-wave devices *Opt. Express* **16** 6216–26

[13] Yang J K, Kee C S and Lee J W 2011 Three-dimensional subwavelength confinement of terahertz electromagnetic surface modes in a coupled slit structure *Opt. Express* **19** 20199–213

[14] Agrawal A, Cao H and Nahata A 2005 Time-domain analysis of enhanced transmission through a single subwavelength aperture *Opt. Express* **13** 3535–42

[15] Lee J W, Seo M A, Sohn J Y, Ahn Y H, Kim D S, Jeoung S C, Lienau C and Park Q H 2005 Invisible plasmonic meta-materials through impedance matching to vacuum *Opt. Express* **13** 10681–7

[16] Seo M A, Adam A J L, Kang J H, Lee J W, Jeoung S C, Park Q H, Planken P C M and Kim D S 2007 Fourier-transform terahertz near-field imaging of one-dimensional slit arrays: mapping of electric-field, magnetic-field and Poynting vectors *Opt. Express* **15** 11781–9

[17] Bulgarevich D S, Watanabe M and Shiwa M 2012 Single sub-wavelength aperture with greatly enhanced transmission *New J. Phys.* **14** 053001

[18] Yu N, Fan J, Wang Q J, Pflügl C, Diehl L, Edamura T, Yamanishi M, Kan H and Capasso F 2008 Small-divergence semiconductor lasers by plasmonic collimation *Nature Photon.* **2** 564–70

[19] Yu N, Wang Q J, Kats M A, Fan J A, Khanna S P, Li L H, Davies A G, Linfield E H and Capasso F 2010 Designer spoof surface plasmon structures collimate terahertz laser beams *Nature Mater.* **9** 730–5

[20] Liu J, Mendis R and Mittleman D M 2012 Designer reflectors using spoof surface plasmons in the terahertz range *Phys. Rev.* B **86** 241405

[21] Mendis R 2006 Guided-wave THz time-domain spectroscopy of highly doped silicon using parallel-plate waveguides *Electron. Lett.* **42** 19–21

[22] Melinger J S, Laman N, Harsha S S and Grischkowsky D 2006 Line narrowing of terahertz vibrational modes for organic thin polycrystalline films within a parallel plate waveguide *Appl. Phys. Lett.* **89** 251110

[23] Melinger J S, Laman N, Harsha S S, Cheng S and Grischkowsky D 2007 High-resolution waveguide terahertz spectroscopy of partially oriented organic polycrystalline films *J. Phys. Chem.* A **111** 10977–87

[24] Laman N, Harsha S S, Grischkowsky D and Melinger J S 2008 High-resolution waveguide THz spectroscopy of biological molecules *Biophys. J.* **94** 1010–20

[25] Awad M M and Cheville R A 2005 Transmission terahertz waveguide-based imaging below the diffraction limit *Appl. Phys. Lett.* **86** 221107

[26] Liu J, Mendis R and Mittleman D M A 2012 Tapered parallel-plate waveguide probe for THz near-field reflection imaging *Appl. Phys. Lett.* **100** 031101

[27] Mbonye M, Mendis R and Mittleman D M 2012 Study of the impedance mismatch at the output end of a THz parallel-plate waveguide *Appl. Phys. Lett.* **100** 111120

[28] Tonouchi M 2007 Cutting-edge terahertz technology *Nature Photon.* **1** 97–105

[29] Nagel M, Haring Bolivar P and Kurz H 2005 Modular parallel-plate THz components for cost-efficient biosensing systems *Semicond. Sci. Technol.* **20** 281–5

[30] Yang B B, Katz S L, Willis K J, Weber M J, Knezevic I, Hagness S C and Booske J H 2012 A high-Q terahertz resonator for the measurement of electronic properties of conductors and low-loss dielectrics *IEEE Trans. Terahertz Sci. Technol.* **2** 449–59

[31] Braakman R and Blake G A 2011 Principles and promise of Fabry–Perot resonators at terahertz frequencies *J. Appl. Phys.* **109** 063102

[32] Chen Y, Al-Naib I A I, Gu J, Wang M, Ozaki T, Morandotti R and Zhang W 2012 Membrane metamaterial resonators with a sharp resonance: a comprehensive study towards practical terahertz filters and sensors *AIP Adv.* **2** 022109

[33] Preu S, Schwefel H G L, Malzer S, Döhler G H, Wang L J, Hanson M, Zimmerman J D and Gossard A C 2008 Coupled whispering gallery mode resonators in the terahertz frequency range *Opt. Express* **16** 7336–43

[34] George P A, Manolatou C, Rana F, Bingham A L and Grischkowsky D R 2007 Integrated waveguide-coupled terahertz microcavity resonators *Appl. Phys. Lett.* **91** 191122

[35] Mendis R, Astley V, Liu J and Mittleman D M 2009 Terahertz microfluidic sensor based on a parallel-plate waveguide resonant cavity *Appl. Phys. Lett.* **95** 171113

[36] Astley V, Reichel K S, Jones J, Mendis R and Mittleman D M 2012 Terahertz multichannel microfluidic sensor based on parallel-plate waveguide resonant cavities *Appl. Phys. Lett.* **100** 231108

[37] Bingham A L and Grischkowsky D 2007 High Q, one-dimensional terahertz photonic waveguides *Appl. Phys. Lett.* **90** 091105

[38] Gerhard M, Imhof C and Zengerle R 2010 Compact three-dimensional terahertz resonators based on periodically corrugated metallic slit waveguides *J. Appl. Phys.* **108** 026102

[39] Williams B S, Kumar S, Callebaut H, Hu Q and Reno J L 2003 Terahertz quantum-cascade laser at $\lambda = 100\,\mu$m using metal waveguide for mode confinement *Appl. Phys. Lett.* **83** 2124–6

[40] Walther C, Scalari G, Amanti M I, Beck M and Faist J 2010 Microcavity laser oscillating in a circuit-based resonator *Science* **327** 1495–7

[41] Strupiechonski E, Xu G, Todorov M B Y, Klang N I A M A P, Sirtori C, Strasser G, Degiron A and Colombelli R 2012 Sub-diffraction-limit semiconductor resonators operating on the fundamental magnetic resonance *Appl. Phys. Lett.* **100** 131113

[42] Deibel J, Escarra M, Berndsen N, Wang K and Mittleman D 2007 Finite element method simulations of guided wave phenomena at terahertz frequencies *Proc. IEEE* **95** 1624–40

[43] Schelkunoff S A and Friis H T 1952 *Antennas, Theory and Practice* (New York: Wiley)

[44] Poincare H and Vreeland F K 1904 *Maxwell's Theory and Wireless Telegraphy* (New York: McGraw-Hill)

[45] Mendis R and Grischkowsky D 2001 Undistorted guided-wave propagation of subpicosecond terahertz pulses *Opt. Lett.* **26** 846

[46] Bonnet C, Chauvat D, Emile O, Bretenaker F, Le Floch A and Dutriaux L 2001 Measurement of positive and negative Goos–Hänchen effects for metallic gratings near wood anomalies *Opt. Lett.* **26** 666–8

[47] Yin X, Hesselink L, Liu Z, Fang N and Zhang X 2004 Large positive and negative lateral optical beam displacements due to surface plasmon resonance *Appl. Phys. Lett.* **85** 372–4

[48] Merano M, Aiello A, t'Hooft G W, van Exter M P, Eliel E R and Woerdman J P 2007 Observation of Goos–Hänchen shifts in metallic reflection *Opt. Express* **15** 15928–34

[49] Bozhevolnyi S I, Volkov V S, Devaux E and Ebbesen T W 2005 Channel plasmon-polariton guiding by subwavelength metal grooves *Phys. Rev. Lett.* **95** 046802

[50] Bozhevolnyi S I, Volkov V S, Devaux E, Laluet J-Y and Ebbesen T W 2006 Channel plasmon subwavelength waveguide components including interferometers and ring resonators *Nature* **440** 508–11